Additive Manufacturing 24 (2018) 647–657

Contents lists available at ScienceDirect

Additive Manufacturing

journal homepage: www.elsevier.com/locate/addma

Full Length Article

Laser-matter interactions in additive manufacturing of stainless steel SS316L and 13-93 bioactive glass revealed by *in situ* X-ray imaging

Chu Lun Alex Leung[a,b], Sebastian Marussi[b,c], Michael Towrie[b,d], Jesus del Val Garcia[e], Robert C. Atwood[f], Andrew J. Bodey[f], Julian R. Jones[g], Philip J. Withers[b,c], Peter D. Lee[a,b,*]

[a] Department of Mechanical Engineering, University College London, Torrington Place, London WC1E 7JE, UK
[b] Research Complex at Harwell, Science & Technology Facilities Council, Rutherford Appleton Laboratory, Oxfordshire OX11 0FA, UK
[c] Henry Royce Institute, School of Materials, The University of Manchester, Oxford Rd, Manchester M13 9PL, UK
[d] Central Laser Facility, Research Complex at Harwell, UK Research & Innovation - Science & Technology Facilities Council, Rutherford Appleton Laboratory, Oxfordshire OX11 0QX, UK
[e] Applied Physics Department, University of Vigo, EEI, Lagoas-Marcosende, Vigo 36310, Spain
[f] Diamond Light Source Ltd, Harwell Science & Innovation Campus, Oxfordshire OX11 0DE, UK
[g] Department of Materials, Imperial College London, South Kensington Campus, London SW7 2AZ, UK

ARTICLE INFO

Keywords:
X-ray imaging
In situ
SS316L
13-93 bioactive glass
Molten pool dynamics

ABSTRACT

Laser-matter interactions in laser additive manufacturing (LAM) occur on short time scales (10^{-6}–10^{-3} s) and have traditionally proven difficult to characterise. We investigate these interactions during LAM of stainless steel SS316L and 13-93 bioactive glass powders using a custom built LAM process replicator (LAMPR) with *in situ* and *operando* synchrotron X-ray real-time radiography. This reveals a wide range of melt track solidification phenomena as well as spatter and porosity formation. We hypothesise that the SS316L powder absorbs the laser energy at its surface while the trace elements in the 13-93 bioactive glass powder absorb and remit the infra-red radiation. Our results show that a low viscosity melt, *e.g.* 8 mPa s for SS316L, tends to generate spatter (diameter up to 250 µm and an average spatter velocity of 0.26 m s^{-1}) and form a melt track by molten pool wetting. In contrast, a high viscosity melt, *e.g.* 2 Pa s for 13-93 bioactive glass, inhibits spatter formation by damping the Marangoni convection, forming a melt track *via* viscous flow. The viscous flow in 13-93 bioactive glass resists pore transport; combined with the reboil effect, this promotes pore growth during LAM, resulting in a pore size up to 600 times larger than that exhibited in the SS316L sample.

1. Introduction

Laser additive manufacturing (LAM) technologies, including laser powder bed fusion (LPBF) [1] and direct energy deposition (DED) [2], fuse loose powder material together using a focused laser beam to build up a three-dimensional (3D) object with complex features, layer upon layer. They offer new design paradigms and product applications across many different sectors, including nuclear fusion [3], aerospace [4] and tissue engineering [5,6].

An entry-level LPBF system comprises a laser system, a powder reservoir and a build chamber that can operate in an inert atmosphere (Fig. 1). It builds either by fusing powder particles on (1) powder (termed an overhang build), or on (2) a solid substrate or a previously built layer (termed layer-by-layer build).

Currently, the adoption of LAM technologies for high-performance structural applications is hindered by many technical challenges, including the control of defects [7] (*e.g.* porosity [8–10]), non-uniform shrinkage [11], poor dimensional accuracy [9,12,13], and surface quality [12]. In addition, LAM parts can display pronounced anisotropy and heterogeneity of microstructure and mechanical properties [14]. Such manufacturing issues may give rise to the failure of LAM components during service [15–17], and hence it is critical to understand the mechanisms by which they form in order to better control them. Recently, Martin et al. [18] introduced inoculants in non-weldable Al-based powders, leading to the formation of fine equiaxed grains, mitigating crack formation during LAM. Wang et al. [19] optimised scan parameters to form low angle grain boundaries inside stainless steel SS316L LAM parts, promoting dislocation pinning and twinning to enhance the material strength. Sun et al. [20] extended previous work by using a high laser power and multi-scan melt pool strategy to form a strong < 011 > crystallographic texture and nano-twins in SS316L parts to increase both strength and ductility.

* Corresponding author at: Department of Mechanical Engineering, University College London, Torrington Place, London WC1E 7JE, UK.
E-mail address: peter.lee@ucl.ac.uk (P.D. Lee).

https://doi.org/10.1016/j.addma.2018.08.025
Received 14 May 2018; Received in revised form 7 August 2018; Accepted 19 August 2018
Available online 23 August 2018

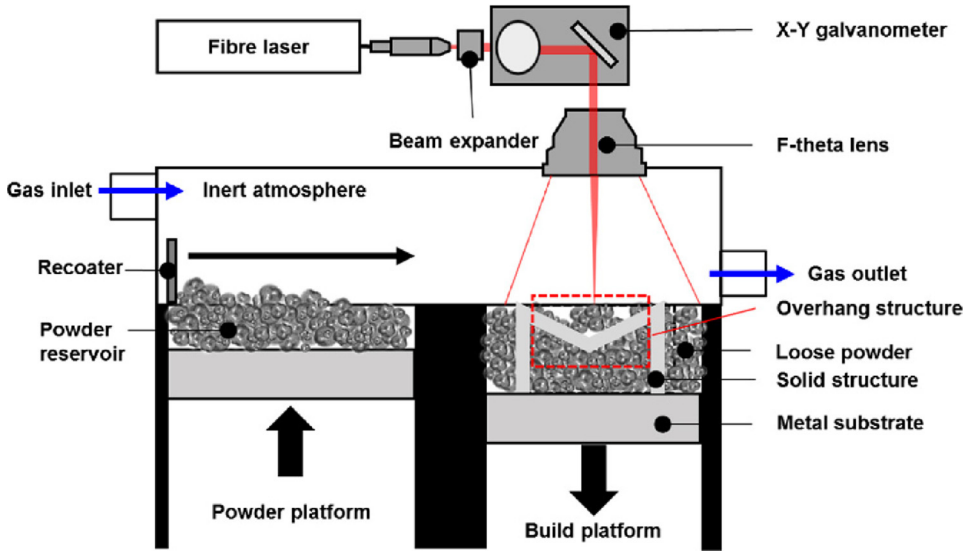

Fig. 1. Schematic of a typical LPBF machine. The build chamber is purged with a flowing inert atmosphere. The blue arrows indicate the gas flow direction.

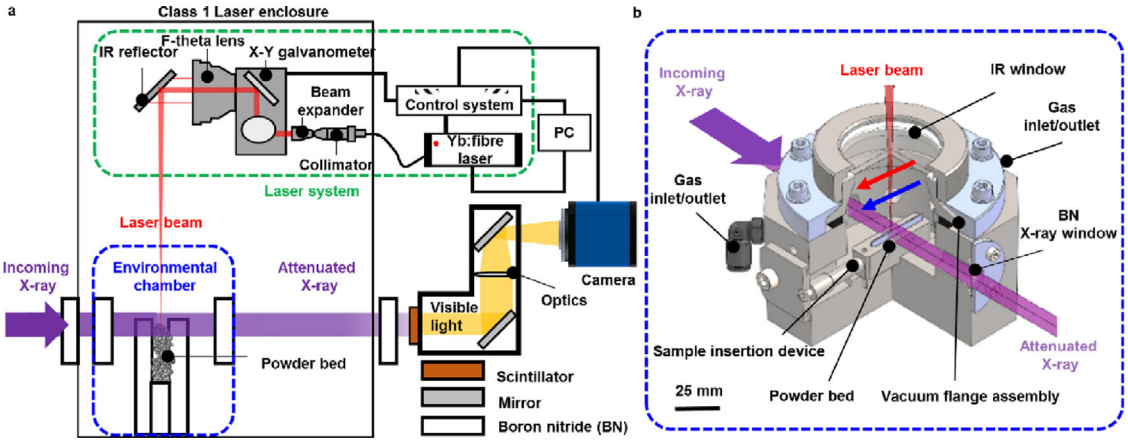

Fig. 2. a, Schematic of the LAMPR mounted on a synchrotron beam line. It comprises three sub-assemblies: 1) a stainless steel environmental build chamber (blue), 2) a laser system (green), and 3) a laser enclosure (black). b, A three-quarter section view of the environmental chamber. The purple arrows indicate the directions of the incoming X-ray beam (dark purple) and the attenuated X-ray beam (light purple). The red arrow indicates the scan direction of the laser beam, which moves parallel along the length of the powder bed. The blue arrow indicates the argon flow direction which is perpendicular to the X-ray beam and parallel to the laser beam.

In recent years, our understanding of additive manufacturing (AM) has improved through *ex situ* destructive (*e.g.* metallography) [21–23] and non-destructive (*e.g.* X-ray computed tomography (XCT) [9,10,12,13]) experiments. However, LAM occurs through an interaction between a laser beam and powder particles, followed by a series of complex powder consolidation phenomena that occur on very short time scales (10^{-6}–10^{-3} s) [24]. These phenomena cannot be studied by *ex situ* characterisation techniques and hence they are not currently well understood [25]. Since the laser-matter interaction and powder consolidation are fundamental to the microstructure and thereby the performance, a better understanding of such interactions is required [26]. A variety of *in situ* real-time measurements [27], including high-speed videography [28–31], Schlieren imaging [32], infrared (IR) thermography [31,33–35], pyrometry [33,36] and electron microscopy [37] have been used to characterise LAM. These *in situ* techniques capture the temperature field and/or images at or above the molten pool surface however they cannot study the changes inside the melt zone, *e.g.* the fluid dynamics and evolution of defects.

Advances in third-generation synchrotron radiation sources [38] make it possible to use a high flux X-ray beam to capture these dynamic processes radiographically at a high spatial (a few micrometres) and temporal (microseconds to milliseconds) resolution [39]. High frame rate radiography has been used to study metal foaming [40], casting [41,42], laser welding [43] and LPBF [44–47], providing additional insights into real-time kinetics, thermodynamics, phase transformations, and transport mechanisms.

Here, a LAM Process Replicator (LAMPR) is accommodated on two high frame rate X-ray imaging beamlines at Diamond Light Source (DLS), UK to study laser-matter interactions and powder consolidation phenomena during LAM of stainless steel SS316L and 13-93 bioactive glass. The SS316L has a near-infrared (NIR) absorption of 64–68% [48,49], a melt viscosity of 8 mPa s, and a solidification range of 1658–1723 K [50]. In contrast to SS316L, 13-93 bioactive glass has a NIR absorptivity of < 1%, a large sintering range between the glass transition and crystallisation onset temperatures (873–963 K) [51], and a melt viscosity of 2 Pa s [52]. Through the study of these very different systems, it is our aim to quantify the effects of chemical, optical and thermophysical properties on the evolution of melt tracks, spatter and porosity and thereby refine our existing understanding of solidification in LAM.

2. Methods

2.1. Technical description of the LAMPR

Our Laser Additive Manufacturing Process Replicator (LAMPR) shown in Fig. 2 is designed to mimic the major features of a typical LPBF system (Fig. 1) while permitting *in situ* and *operando* imaging of the laser-matter interaction and powder consolidation phenomena with synchrotron X-rays. It is a compact, lightweight (*ca.*15 kg) and portable device that can be integrated into different synchrotron X-ray imaging and diffraction beamlines (Fig. 2a). The environmental build chamber and laser enclosure are each equipped with two circular boron nitride (BN) X-ray translucent windows (10 mm in diameter and 0.25 mm thick) to permit X-rays to interact with the sample (Fig. 2b). In order to capture the evolution of the melt track in steady and non-steady states, the size of the X-ray windows is larger than the field of view (FOV) of the imaging setup available at the synchrotron beamlines. In this study we focus on the overhang build configuration [26], using a powder bed (30 mm long, 3 mm deep and 0.3 mm thick) contained by three BN plates (each plate is 0.3 mm thick) stacked next to each other, in which the middle plate is 3 mm shorter than the others (see inset image in Fig. 2). For layer-by-layer AM build conditions, the middle plate is replaced by a metal substrate with a suitable height to match the thickness of a single powder layer.

Boron nitride is often used for high temperature and X-ray imaging applications [53,54] and hence is used for all components in the X-ray beam path (giving a total transmitted thickness of 1.6 mm). This gives an overall X-ray transmission of > 90% between 20–150 keV, providing excellent image contrast of the sample. Furthermore, BN is not wet by most molten metals or slag, *i.e.* glass, allowing reuse of the sample holder. Alternatively, glassy carbon and Kapton™ may be used for the external X-ray windows due to their low X-ray absorption and amorphous structures, which make them well suited for X-ray imaging and diffraction studies [44].

The sample is placed into the environmental build chamber *via* the side port (Fig. 2b). This is designed for precision alignment of the powder bed to the focal position of the laser beam, and to be perpendicular to the X-ray beam. All the connected components are either sealed with O-rings or standard vacuum flanges, thus enabling the environmental build chamber to maintain a vacuum pressure of 10^{-3} Torr or support different gas flow environments at a pressure of 760 Torr. The IR window has a high transmission percentage of 95% across a wavelength range of 0.3–6 µm which permits the laser beam and light reflections from the powder bed to pass through. This enables the LAMPR to perform correlative optical imaging and thermography at the powder bed surface while imaging the internal structure of the melt track during LAM with X-rays.

The laser system consists of an ytterbium-doped fibre laser (wavelength of 1070 nm, transverse mode $TEM_{00,}$ continuous-wave (CW), beam quality factor (M^2) of 1.03, power (P) of 200 W (SPI Lasers Ltd, UK)), a beam expander, Infra-red (IR) reflective optics, and a Class 1 laser safety enclosure (compliant with EN60825-4). The diameter of the collimated laser beam is increased from 5 to 10 mm *via* a beam expander before entering into an X-Y galvanometer (Laser control systems Ltd., UK). The X-Y galvanometer is capable of moving the 200 W laser beam at a scan velocity (v) of 4 m s^{-1}. Lastly, the laser beam is focused down to a 50 µm diameter spot at a focal distance of 254 mm (or at the powder bed surface) *via* an f-theta lens and an IR reflector. The LAMPR is synchronised with the image acquisition system in the synchrotron beamlines for *in situ* and *operando* X-ray imaging in real and reciprocal space.

2.2. Materials

To better understand the effects of powder properties on laser absorption mechanisms, melt flow behaviour, and the evolution of the melt track and defects (*e.g.* spatter and porosity), we chose two powders with large differences in chemical, optical and thermophysical properties. The two powders were: (1) a gas atomised stainless steel (SS316L) powder (Sandvik Osprey Ltd., Sweden); and (2) a melt-quenched 13-93 bioactive glass powder ($6Na_2O$-$12K_2O$-5MgO-20CaO-$4P_2O_5$-$53SiO_2$; wt%). The 13-93 bioactive glass composition was chosen because it has a large sintering window (between the glass transition temperature and the onset of crystallisation temperature), which means it can be sintered without crystallisation (unlike the original 45S5 Bioglass).

The 13-93 bioactive glass was fabricated using a melt quenching route described elsewhere [6,55,56]. Precursors of SiO_2 (Prince Minerals, Stoke-on-Trent), $MgCO_3$, P_2O_5, $CaCO_3$, Na_2CO_3 and K_2CO_3, all with a purity > 96% (Sigma-Aldrich, UK), were mixed together using a Wheaton bench-top small bottle roller for 3 h to ensure homogeneity. The mixture of oxides and carbonates was melted at 1400 °C in a platinum (Pt/Au 95/5) crucible for 90 min. and quenched in deionized water. The frit was dried at 120 °C for 24 h and ball milled for 30 min. at 500 rpm (Premium Line 7 ball mill, Fritsch GmbH, Germany). Finally, the powder was sieved for 60 min at 2 mm of amplitude (Vibratory Sieve Shaker Analysette 3 Pro, Fritsch GmbH, Germany) to discard any particles having a diameter greater than 150 µm.

Powder morphology was characterised by scanning electron microscopy (SEM, JEOL JSM-6610LV, Japan). The particle size distribution (PSD) of both powders was determined from the SEM images using segmentation and object identification routines in the Image Processing Toolbox in MATLAB 2016a (Mathworks, USA). The SS316L composition was examined by Energy-Dispersive Spectroscopy (EDS). The 13-93 bioactive glass composition was characterised by inductively coupled plasma optical emission spectroscopy (ICP-OES, Optima 4300 DV, Perkin Elmer, USA) following lithium metaborate fusion. After ball milling, we performed X-ray Fluorescence (XRF) to examine the trace compounds of the 13-93 bioactive glass. The diffuse reflectance (%) of the 13-93 bioactive glass was measured by UV-VIS-NIR spectrophotometer with an integrating sphere attachment (UV-2600 and IRS-2600 plus, Shimadzu Corporation, Japan). The spectrum was calibrated using a white barium sulphate standard. The Kubelka-Munk function, $\boldsymbol{F(R)}$ is often used to correlate the diffuse reflectance ($\boldsymbol{R}$) to the absorbance of the 13-93 bioactive glass [57]. $\boldsymbol{F(R)}$ is a ratio of the absorption coefficient ($\boldsymbol{K}$) and scattering coefficient ($\boldsymbol{S}$) of the powder:

$$\boldsymbol{F(R)} = \frac{(1-\boldsymbol{R})^2}{2\boldsymbol{R}} = \frac{\boldsymbol{K}}{\boldsymbol{S}} \quad (1)$$

2.3. In situ and operando synchrotron X-ray radiography setup

To observe the laser-matter interaction and powder consolidation process, we performed LAM trials on SS316L using the LAMPR and the imaging setup of Joint Engineering Environment and Processing (JEEP) beamline (I12) and the Diamond-Manchester Imaging Branchline (I13-2) to study LAM of 13-93 bioactive glass. The imaging parameters are summarised in Table 1. Both beamlines are located at Diamond Light Source, UK.

Both experiments were performed using overhang configurations (Fig. 1). A laser beam scanned a 4 mm line across the powder bed of SS316L (with a nominal $P = 150$ W and $v = 5\,\mathrm{mm\,s^{-1}}$) and 13-93 bioactive glass (with a nominal $P = 20$ W and $v = 5\,\mathrm{mm\,s^{-1}}$) in an argon atmosphere at a flow rate of $4\,\mathrm{l\,min^{-1}}$. The scan velocity was selected to enable the formation of a continuous track under overhang configurations [45]. The image acquisition system was synchronised with the LAMPR using a ring buffer mode that continuously recorded images at 5100 frames per seconds (fps) into the on-board memory of the camera until the laser was triggered. These images were captured into digital images *via* a 700 µm thick LuAg: Ce scintillator (at I12) and a 500 µm thick $ZnWO_4$ scintillator (at I13-2). Before the laser trigger point, 100 images were recorded as flat field images, and then a further

Table 1
Key characteristics of the synchrotron X-ray imaging systems used for this study.

Beamline	I12: JEEP	I13-2
Energy range (keV)	55 (Monochromatic)	5–35 (Pink)
CCD camera	Miro 310 M (Vision Research, US)	PCO.dimax S4 (PCO Group GmbH, Germany)
Sensor size (pixels)	1280 × 800	2016 × 2016
Bit depth	12-bit	12-bit
Field of view (mm)	8.4 × 3.3 (Region of interest mode)	6.5 × 2.5 (Region of interest mode)
Effective pixel size (μm)	6.6	5.5
Acquisition speed (fps)	5100	5100

100 dark field images were taken without switching on the X-ray beam.

2.4. Post-mortem X-ray computed tomography (XCT)

After the *in situ* radiography experiments, both melt tracks were examined by a laboratory X-ray computed tomography (XCT) system, Nikon XTH 225 X-ray microfocus system (Nikon, Japan), using the acquisition parameters in Table 2. We then reconstructed the XCT scan into a 3D image volume using built-in beam hardening correction and filtered back projection algorithms in CT Pro3D (Nikon, Japan).

2.5. Image processing and quantification

Using the image processing and quantification procedure defined in our previous study [45], we applied a flat field correction and the VBM3D denoising algorithm [58] in MATLAB 2016a to improve the signal to noise ratio of the acquired images. This was followed by a custom background subtraction and image thresholding techniques to extract the evolution of melt features, which enables the quantification of the molten pool geometries over time, including the length, width, and area. For the SS316L dataset, we tracked some of the spatter droplets using the Manual Tracking plugin from ImageJ [59] and quantified their velocities [45]. We also measured the spatter size using the oval tool in ImageJ.

For the XCT dataset, we quantified the pore size distribution of both melt tracks in 3D using Avizo 9.1 (Thermo Fisher Scientific, US) and the method described in the literature [12,60]. We discarded any segmented objects with a volume fewer than five voxels (equivalent to a diameter of 6.75 μm) to minimise quantification errors induced by image noise.

3. Results

3.1. Powder characterisation

Fig. 3 shows the characteristics of the SS316L and 13-93 bioactive glass powders. The SS316L powder particles are mostly spherical though some are slightly elongated (Fig. 3a) whereas the 13-93 powder particles exhibit an irregular shape (Fig. 3b). The particle size distributions are 30–105 μm for SS316L and 5–140 μm for 13-93 bioactive glass (Fig. 3c). The median particle diameters (d_{50}) for SS316L and 13-93 bioactive glass are 43 μm and 38 μm, respectively.

Given that the penetration depth of EDS is < 5 μm, the oxygen detected by EDS is mainly associated with the thin oxide layer at the SS316L powder surface. As a consequence, we neglected the oxygen content and normalised the elemental compositions of the SS316L powder (Table 3).

The ICP-OES and XRF results (Table 4) show the composition of a typical 13-93 bioactive glass; however, the XRF results indicate that the 13-93 bioactive glass exhibit trace compounds of Fe_2O_3, Al_2O_3, TiO_2, and SiO_3 after ball milling. The $\boldsymbol{F}(\boldsymbol{R})$ of 13-93 bioactive glass (Fig. 3d) indicates that the glass powder had a high absorbance at the wavelength of the laser beam compared to the rest of the spectrum.

3.2. In situ observation of LAM deposition of a SS316L track

A montage of time-series radiographs shows the evolution of SS316L melt features from a cross-sectional view of the powder bed during LAM; see Fig. 4 and Supplementary Movie S1. At the onset of LAM, the laser beam scans from right to left across the powder bed, forming an initial molten pool at the right-hand side of the powder bed. The molten pool grows rapidly into a sphere; however, its growth rate slows substantially as it reaches an area equivalent diameter of 500 μm (at 22 ms). At 63 ms, the laser scan velocity surpasses the growth rate of the initial melt bead such that the laser beam forms a new molten pool 50 μm ahead of the first melt bead. At 146 ms, the new molten pool coalesces with the previous melt bead to form a melt track. This process of forming new, separate, molten pools ahead of the main track continues until 280 ms, with each subsequently coalescing into the main melt track (**green circle**). By 350 ms, these large molten pools completely merge with the main melt track (**green circle**), extending the track length to form a continuous layer. At 518 ms, the melt track begins to cool and contract.

At the onset of LAM, the molten pool rises *ca.* 50 μm above the powder layer, this is possibly due to (1) the molten pool geometry being larger than the width of the powder bed (300 μm), and thus the molten pool is trapped between the BN walls; (2) the intense laser beam (with a laser power density of 10^6 W/cm^2) causes metal vapourisation at the melt surface, generating a recoil pressure at the laser-matter interaction zone. Therefore, the surrounding argon gas is conductively heated and combined with the metal vapour; expanding as a gas/vapour jet upwards and outwards at high speed. This generates lift forces to keep the molten pool away from the powder layer.

In some cases, these lift forces are sufficient to induce powder and droplet spatter (**blue dotted circles at 63** and **146 ms**), forming a denuded zone [61]. We tracked 13 typical spatter droplets, with equivalent diameters varying between 33 μm and 250 μm. The average and maximum spatter velocities are 0.16 m s^{-1} and 0.26 m s^{-1}, respectively. The radiographs and Supplementary Movie S1 indicate that the spatter trajectories depend strongly on the directions of the gas flow and scanning laser beam. Spatter and metal vapourisation remove powder particles from the laser-matter interaction zone, whilst powder consolidation further reduces the amount of powder ahead of the scan path; all contribute to the enlargement of the denuded zone. These factors reduce the growth rate and volume of the molten pool, and hence reduce the final melt track size.

During LAM, the temperature at the centre of the molten pool is expected to be much higher than that at the edges of the molten pool, this induces a thermal gradient across the molten pool surface. The melt moves away from the centre of the molten pool (*i.e.* a low surface tension region) to the edges of the molten pool (*i.e.* a high surface

Table 2
The XCT scan parameters.

Sample	Accelerating voltage (kV)	Beam current (μA)	Number of projections	Exposure time (ms)	Scan volume (mm^3)	Voxel size (μm^3)
SS316L	100	80	3142	500	5.4	2.7
13-93 bioactive glass	50	130	3142	500	5.4	2.7

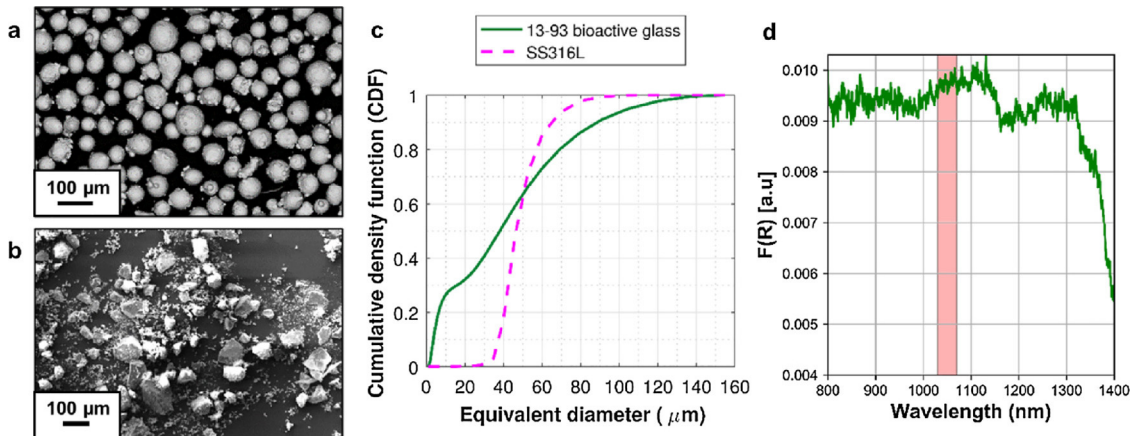

Fig. 3. SEM images of (a) SS316L metallic powder and (b) 13-93 bioactive glass powder. (c) Particle size distributions. (d) Diffuse reflectance of 13-93 bioactive glass powder in Kubelka-Munk unit or $\boldsymbol{F(R)}$. The red region indicates the wavelength of the laser beam.

Table 3
Normalised elemental composition of the SS316L powder obtained by EDS.

Elemental compositions of SS316 (weight %)									
Fe	Cr	Ni	Mo	Mn	Si	Co	Nb	S	P
65.9 ± 0.4	17.8 ± 0.2	11.7 ± 0.2	2.2 ± 0.3	0.8 ± 0.1	0.7 ± 0.1	0.4 ± 0.2	0.2 ± 0.2	0.2 ± 0.1	0.1 ± 0.1

Table 4
Chemical composition of the 13-93 bioactive glass obtained by ICP and XRF.

Method	Chemical compositions (weight %)									
	SiO2	CaO	K_2O	MgO	Na_2O	P_2O_5	Al_2O_3	SO_3	TiO_2	Fe_2O_3
ICP	53.0	20.0	12.0	5.0	6.0	3.9	–	–	–	–
XRF	50.1	22.7	10.6	5.0	6.2	5.0	0.19	0.07	0.05	0.05

tension region) to reduce the overall free energy, inducing Marangoni-driven melt flow [62]. When new molten pools form ahead of the melt track, the resultant Marangoni forces cause them to migrate in a direction opposite to the direction of the scanning laser beam, facilitating molten pool wetting onto the melt track (**green dotted circle**, Fig. 4). These observations suggest that molten pool wetting is a key mechanism for track formation and growth during LAM of SS316L in the overhang condition. Similar mechanisms have been reported in Invar 36 [45], further supporting this hypothesis.

3.3. *In situ* observations of LAM deposition of a 13-93 bioactive glass track

A montage of time-series radiographs shows the evolution of 13-93 bioactive glass during LAM in Fig. 5 (and Supplementary Movie S2). After 8 ms, the laser beam fuses the glass powder into a molten glass bead at the right-hand side of the powder bed. At 22 ms, the molten glass bead grows larger with spherical gas pores forming inside the glass bead with an area equivalent diameter of 50 μm. By 30 ms, some of the gas pores inside these molten glass beads grow at the expense of others *via* coalescence. At 60 ms, the molten glass bead grows into a large 700 μm bead by merging with neighbouring molten glass beads

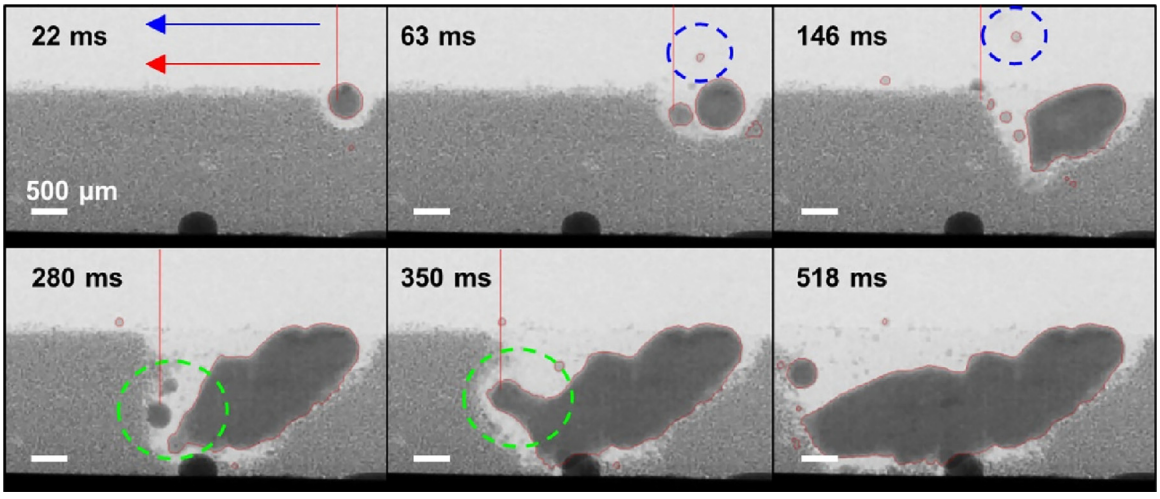

Fig. 4. Typical time-series radiographs (see also Supplementary Movie S1) showing melt track evolution during SS316L LAM ($P = 150$ W and $v = 5$ mm s^{-1}). Directions of the laser beam (red arrow) and gas flow (blue arrow) are shown in the 22 ms frame. The overlaid vertical red lines indicate the laser beam position as it moves from right to left. Red outlines highlight tracked and quantified objects. Blue circles highlight the droplet spatter movement. Green circles show track growth *via* molten pool wetting.

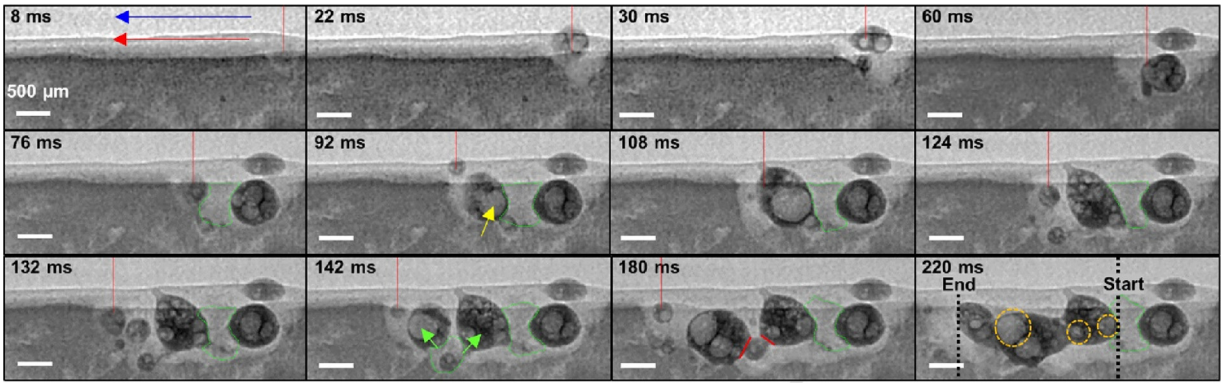

Fig. 5. Time-series radiographs (see also Supplementary Movie S2) show the mechanisms of track formation during 13-93 bioactive glass LAM (P = 20 W and v = 5 mm s^{-1}). Directions of the laser beam (red arrow) and gas flow (blue arrow) are shown in the 8 ms frame. Vertical red lines indicate the laser beam position. The yellow arrow indicates a growing gas pore. Green dotted lines highlight the glassy film and green arrows highlight the movement of the lower glass sphere. Dark red lines show the necks between three spheres. Orange dotted circles highlight pores that stop growing after pore coalescence. Black dotted lines indicate that only a section of the track length is being measured.

and powder particles [63]. Concurrently, the first melt bead residing at the top of the powder bed stops growing. As LAM progresses, similar to the SS316L, new molten glass beads form separately ahead of the existing beads (76 ms). Internal pores also form in these new beads, growing as before. At 92 ms, several pores coalesce into a single large pore with a diameter of 600 µm **(yellow arrow)** in the new molten bead, dramatically increasing its volume. At 124 ms, the large gas pore bursts open. However, the molten bead remains the same size and its internal structure retains many spherical pores. During 124–132 ms, some of these internal pores continue to coalesce and merge into larger pores while others stop growing, suggesting that the bead is cooling.

After 108 ms a glassy film starts to form, creating a bridge between the second and third melt beads **(see the green dotted line)**. At 142 ms, another glassy film appears (**green dotted line**), wrapping around the lower sphere and connecting to the two adjacent spheres. From 142 to 180 ms, this glassy film pulls the bottom sphere upwards (**highlighted by the green arrows**), bringing the molten glass spheres into contact with each other. At 180 ms, necks form between these spheres (**red lines**) and the glassy film becomes a part of a continuous glass track. Between 180–220 ms, the viscous flow of the molten glass continues to promote neck growth, forming a contiguous melt track for most of the scan length. The driving force for neck growth is by reducing the curvature of the neck surfaces and minimising the Gibbs free energy of the system. These observations confirm that the viscous flow is a main track formation mechanism for 13-93 bioactive glass.

3.4. Time-resolved quantification of SS316L and 13-93 bioactive glass melt tracks

The *in situ* observations show the dynamic evolution of melt features during LAM, including the formation of melt tracks, denuded zones, pores and spatter. Using these radiographs, we have quantified the evolution of melt track geometry and area shrinkage (%) for SS316L and 13-93 bioactive glass (see Fig. 6).

The track length of the SS316L sample is 4.6 mm, *ca.* 15% longer than the nominal scan length of 4 mm (Fig. 6a). This is because the heat affected zone is always larger than the laser spot size, hence the melt track is expected to be longer than the nominal scan length. The elongation of the melt track may also be constrained by the BN walls. In contrast, the track length of the 13-93 bioactive glass sample is 2.8 mm, *ca.* 40% shorter than the nominal track length, due to the glassy film at the front-end of the track breaking apart during sample handling, thus the front end of the track is excluded in this quantification. The overall track length, including the glass film and beads, is *ca.* 6.3 mm.

Fig. 6b shows that the SS316L and the 13-93 bioactive glass undergo a maximum shrinkage of 6.4 % and 3.2 % during LAM, respectively. The coefficient of expansion (CTE) of SS316L is at 19.5 × 10^{-6} K^{-1} at 200–1000 °C [64] whereas the CTE of 13-93 bioactive glass is *ca.* 12.5 × 10^{-6} K^{-1} at the glass transition temperature (*ca.* 600 °C) [65]. This is in accordance with our results which show that SS316L can contract ~50% more than 13-93 bioactive glass during cooling.

Fig. 6c shows that the measured spatter velocity is inversely proportional to the size of the spatter droplet, reducing from 0.26 m s^{-1} to 0.05 m s^{-1} as the equivalent diameter (D_{eq}) increases from 33 µm to *ca.* 250 µm, matching the trend reported by Ly et al. [66]. The weight of the spatter and the vapour induced recoil force on the spatter surface increases proportionally with D_{eq}^3 and D_{eq}^2, respectively, therefore we would expect the spatter velocity to decrease with increasing D_{eq}.

3.5. Ex situ analysis by X-ray computed tomography

One drawback of 2D radiographic imaging is that all the melt features are overlaid along the X-ray beam path, making it difficult to interpret whether gas pores/glassy films are connected or just lie in front or behind each other. Therefore we performed XCT to reveal the internal structure and connectivity of these melt tracks, enabling quantification of porosity and other features in 3D (Fig. 7a–c) [12,60].

The total percentage porosity in the SS316L melt track is 0.03 vol%, indicating that the LAMPR is capable of producing high density SS316L melt tracks under overhang conditions. Of this tiny amount of porosity, 80% is open pores that connect to the surface, while only 20% is closed. The majority of closed pores have a D_{eq} of 10 ± 2 µm, with the largest having a D_{eq} of 27 µm. These closed pores in SS316L are likely to be gas pores on account of their spherical shape (Fig. 7a) and small size (Fig. 7c) [67].

The 13-93 bioactive glass track has a porosity of 17.6 vol%, which is 600 times greater than that of SS316L, see Fig. 7b and c. Of the porosity, 82% is open pores and 18% is closed pores. The closed pores are spherically shaped and have an average D_{eq} of 260 µm. The largest open pore in the 13-93 bioactive glass track has a D_{eq} of 530 µm whereas the largest open pore in SS316L has a D_{eq} of 83 µm. Overall, the 13-93 bioactive glass track has pores with a diameter 5–10 times larger than those in SS316L, suggesting that the mechanisms driving pore nucleation and growth are very different during LAM of 13-93 bioactive glass as compared to SS316L.

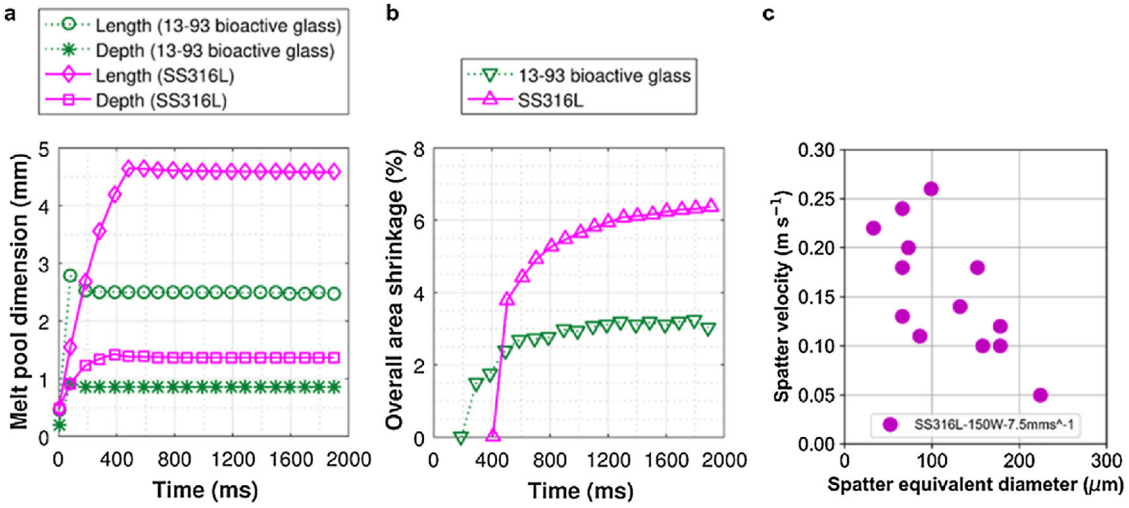

Fig. 6. Time-resolved quantification of (a) molten pool geometry, (b) area shrinkage, and (c) spatter velocity (SS316L only).

4. Discussion

4.1. Laser absorption mechanisms

This study reveals the very different melt behaviour of stainless steel SS316L and 13-93 bioactive glass powders during LAM. For SS316L, the powder particles absorb approximately 68% of the laser beam's energy at a wavelength of 1000 nm [48,49] *via* electron-electron and electron-photon interactions [68], heat energy is transferred across the powder bed *via* conduction.

For the 13-93 bioactive glass, its major constituents (SiO_2, MgO [69] and P_2O_5 [70]) exhibit minimal absorption in the NIR range; however, the $\boldsymbol{F}(\boldsymbol{R})$ results show that the 13-93 bioactive glass has a much higher absorbance than expected owing to the presence of transition metal oxides (TMOs), such as TiO_2 [71] and Fe_2O_3 [72]. The TMOs absorb and re-emit the IR radiation, combining with multiple reflections (or scattering) of IR radiations, promote the NIR absorption and melting of 13-93 bioactive glass as shown by Fig. 8.

4.2. Mechanisms of melt track evolution

As shown in Figs. 4 and 5, the melt track formation of SS316L is mainly driven by molten pool wetting whereas the melt track formation of the 13-93 bioactive glass track is driven by viscous flow (or viscous merging [73]). As the laser beam scans across the molten pool of SS316, the Marangoni-driven flow causes the molten pool to move opposite to the laser scanning direction; thus, the molten pool coalesces onto the solidified beads to form a melt track. We have observed a different mechanism during LAM of 13-93 bioactive glass. The radiography results show the 13-93 bioactive glass undergoes viscous flow, suggesting that the temperature of the glass is near the glass transition temperature (*ca.* 600 °C [74]). At this temperature, the viscosity remains high that strong Marangoni-flow in the 13-93 bioactive glass does not occur. Henceforth, the track formation of 13-93 bioactive glass is driven by forming necks between glass beads, minimising the overall surface energies of the process.

4.3. Pore evolution mechanisms

Both melt tracks contain many spherical closed pores (Fig. 7). In general, pore formation is due to three main factors: (1) exsolution of dissolved gas, (2) inadequate liquid feeding upon solidification, and (3) entrainment of insoluble gas (*e.g.* lapping). In terms of the first, exsolution of dissolved gases such as hydrogen [8,41], the gas can either be present in the powder particles [75], formed by dissociation of adsorbed moisture on the powder surface or be absorbed from the cover gas in the environmental build chamber during LAM. In the 13-93 bioactive glass study, we postulate that the laser-glass powder interaction produces low boiling point volatiles (*e.g.* Na, K, and Mg) inside the molten glass which also promotes pore formation, *i.e.* the 13-93 bioactive glass undergoes reboiling [76].

For the SS316L build, the large open pores were formed by the coalescence of small closed pores to minimise their surface energy which then burst open at the surface. This happens either during the final solidification stages, and hence the surface freezes, forming a surface depression or a dent at the same location [45], or the depression may be stabilised by an oxide film. Either way an open pore is formed [45,77], see inset of Fig. 7a. By contrast, the formation mechanism of open pores in LAM of 13-93 bioactive glass is different from that in metallic alloys. The viscous flow movement induces a shear stress that overcomes the surface tension of the molten glass, breaking open the closed pore, and forming an open one. These open pores are retained as indents after pore bursting as shown in Fig. 5 at 220 ms and Fig. 7b.

In addition to pore formation, growth and collapse during LAM of SS316L, the Marangoni-driven melt pool flow can facilitate pore migration, entraining gas pores and transporting them to different locations inside the melt track; *e.g.* near the top surface or at the bottom of the melt track [45]. We also observed that flow facilitated pore coalescence, forming many pores [45]. Although some pores were swept to the surface by the Marangoni-driven flow and released into the atmosphere, many did not burst and were retained in the solid near the melt track surface after solidification. We postulate that these pores are trapped in the rapidly growing dendrites, being pinned between them [78].

In contrast, the high viscosity of the 13-93 bioactive glass substantially restricts pore migration by dampening the Marangoni-driven flow. This facilitates pore coalescence and bursting. Viscou flow, reboiling, and vitrification of the 13-93 bioactive glass all promote pore growth, resulting in a much higher pore fraction of large pores than in SS316L (Fig. 7b and c).

A significant amount of powder and droplet spatter was observed during SS316L LAM caused by Marangoni-driven flow combined with metal vapour and argon gas induced recoil pressure. Conversely, no spatter is evident during LAM of the high viscosity 13-93 bioactive glass. At the melting temperature of both samples, the viscosity of the molten 13-93 bioactive glass (2 Pa s) [52] is *ca.* 250 times higher than the viscosity of the molten SS316L (0.008 Pa s) [50]. The 13-93 bioactive glass's high viscosity dampens Marangoni-driven flow, reducing spatter formation, supporting the hypothesis of Khairallah et al. [79] that increasing molten pool viscosity could possibly reduce spatter

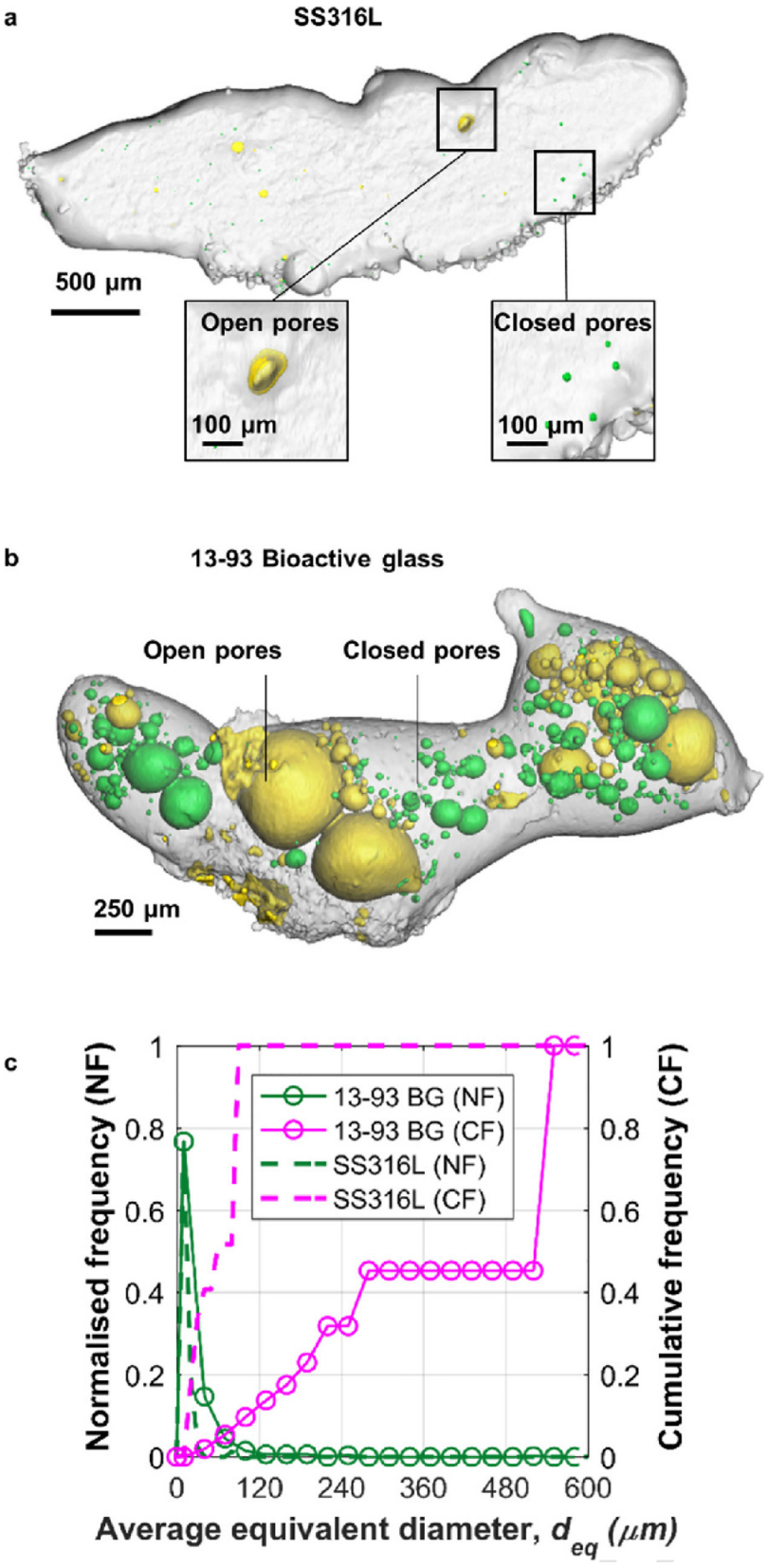

Fig. 7. XCT porosity analysis of SS316L and 13-93 bioactive glass melt tracks. 3D surface rendered images of (a) SS316L and (b) 13-93 bioactive glass melt tracks overlaid with closed pores (green) and open pores (yellow). (c) Pore size distribution of both melt tracks.

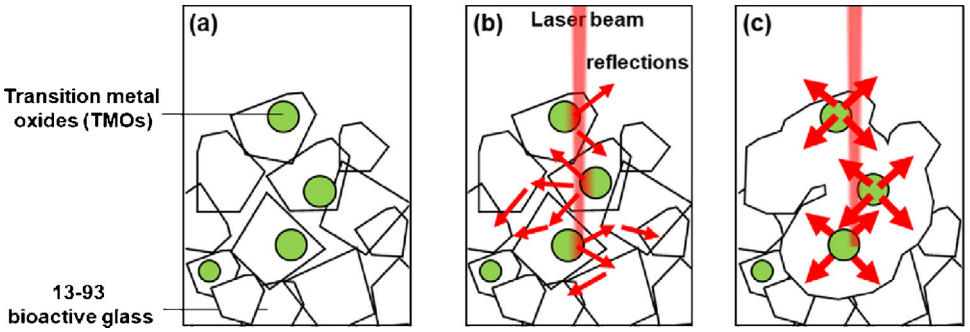

Fig. 8. Schematic showing the laser melting sequence of 13-93 bioactive glass: (a) the TMOs in the 13-93 bioactive powder (b) absorbs a portion of the laser beam during LAM. The other portion of the laser beam was reflected by the powder surfaces. (c) The TMOs re-emit the absorbed radiation which heats up the rest of the powder particles, the residual heat conducts to the surrounding powder particles. The combination of (b) multiple reflections and (c) the re-emission of IR radiations from the TMOs promote the melting of 13-93 bioactive glass.

in LAM.

Direct [80–83] and indirect (with binder materials) [84,85] LAM of glass powders has previously been demonstrated using CO_2 lasers (10.6 μm); however, to the best of our knowledge, it has not been done using a NIR laser. Our results demonstrate that direct LAM of 13-93 bioactive glass is possible without a binder, opening a window for LAM of bioactive glasses using NIR laser beams.

5. Conclusions

A custom-built LAMPR was integrated into two synchrotron X-ray imaging beamlines allowing the laser-matter interaction and powder consolidation of stainless steel SS316L and 13-93 bioactive glass during LAM to be investigated.

It appears that SS316 powder absorbs the laser energy at its surface, which transforms into heat energy and subsequently conducts to the rest of the powder bed whilst 13-93 bioactive glass absorbs much of the laser energy *via* absorption and re-emission of IR radiation and multiple IR reflections stimulated by the presence of transition metal oxides.

In situ real-time radiography reveals that the melt track formation mechanisms of SS316L and 13-93 bioactive glass are driven by molten pool wetting and viscous flow, respectively. It also shows that a low viscosity melt, *e.g.* SS316L, tends to form droplet spatter during LAM due to the strong Marangoni-driven flow. The Marangoni-driven flow also promotes pore transport and gas release into the atmosphere, therefore the SS316L track only exhibits 0.03% porosity.

Conversely, a high viscosity melt, *e.g.* 13-93 bioactive glass, prevents spatter formation during LAM by damping Marangoni-driven flow. The viscous flow behaviour of 13-93 bioactive glass restricts pore transport, in combination with the reboil effect, facilitates pore coalescence and growth. Consequently, the 13-93 bioactive glass track exhibited 17.6% porosity, *ca.* 600 times higher than that in SS316L track. Lastly, we reveal that the formation of open pores in LAM of 13-93 bioactive glass is due to pore bursting.

Data availability

Representative samples of the research data are given in the figures (and Supplementary data – https://doi.org/10.1016/j.addma.2018.08.025). Other datasets generated and/or analysed during this study are not publicly available due to their large size but are available from the corresponding author on reasonable request.

Declaration of interest

The authors declare no competing financial interests.

Acknowledgements

The authors acknowledge financial support from the AMAZE (Additive Manufacturing Aiming towards Zero Waste and Efficient Production of High-Tech Metal Products) project funded by the 7th Framework Programme of the European Commission (contract FP7-2012-NMP-ICT-FoF-313781), the EPSRC-UK MAPP Future Manufacturing Hub (EP/P006566/1, www.mapp.ac.uk), and grants (EP/I02249X/1 and EP/M009688/1). We also acknowledge the use of facilities and support provided by the Research Complex at Harwell and thank Diamond Light Source for providing the beamtime (proposal numbers: EE13641-1 and MT15250-1) and staff (including Dr. Kazimir Wanelik and Andrew A. Wilson) at both beamlines for their technical assistance. We also thank group members (particularly Dr. Enyu Guo and Dr. David Eastwood) for their assistance in this beamtime, and Professor Ken Mills for stimulating and enlightening conversations.

Appendix A. Supplementary data

Supplementary material related to this article can be found, in the online version, at doi:https://doi.org/10.1016/j.addma.2018.08.025.

References

[1] ASTM F42.91, F2792-12a: standard terminology for additive manufacturing technologies, ASTM Int. (2012) 1–3, https://doi.org/10.1520/F2792-12A.
[2] I. Gibson, D.W. Rosen, B. Stucker, 1st ed., Additive Manufacturing Technologies: Rapid Prototyping to Direct Digital Manufacturing vol. 17, Springer Science/Business Media, New York, 2010.
[3] Y. Zhong, L.-E. Rännar, L. Liu, A. Koptyug, S. Wikman, J. Olsen, D. Cui, Z. Shen, Additive manufacturing of 316L stainless steel by electron beam melting for nuclear fusion applications, J. Nucl. Mater. 486 (2017) 234–245, https://doi.org/10.1016/j.jnucmat.2016.12.042.
[4] T.M. Pollock, Alloy design for aircraft engines, Nat. Mater. 15 (2016) 809–815, https://doi.org/10.1038/nmat4709.
[5] S.Y. Chin, Y.C. Poh, A.-C. Kohler, J.T. Compton, L.L. Hsu, K.M. Lau, S. Kim, B.W. Lee, F.Y. Lee, S.K. Sia, Additive manufacturing of hydrogel-based materials for next-generation implantable medical devices, Sci. Robot. 2 (2017) eaah6451, , https://doi.org/10.1126/scirobotics.aah6451.
[6] J.R. Jones, Review of bioactive glass: from Hench to hybrids, Acta Biomater. 9 (2013) 4457–4486, https://doi.org/10.1016/j.actbio.2012.08.023.
[7] B. Zhang, Y. Li, Q. Bai, Defect formation mechanisms in selective laser melting : a review, Chin. J. Mech. Eng. 30 (2017) 515–527, https://doi.org/10.1007/s10033-017-0121-5.
[8] N.T. Aboulkhair, N.M. Everitt, I. Ashcroft, C. Tuck, Reducing porosity in AlSi10Mg parts processed by selective laser melting, Addit. Manuf. 1 (2014) 77–86, https://doi.org/10.1016/j.addma.2014.08.001.
[9] C. Qiu, S. Yue, N.J.E. Adkins, M. Ward, H. Hassanin, P.D. Lee, P.J. Withers, M.M. Attallah, Influence of processing conditions on strut structure and compressive properties of cellular lattice structures fabricated by selective laser melting, Mater. Sci. Eng. A 628 (2015) 188–197, https://doi.org/10.1016/j.msea.2015.01.031.
[10] F. Léonard, S. Tammas-williams, P.B. Prangnell, I. Todd, P.J. Withers, Assessment by X-ray CT of the effects of geometry and build direction on defects in titanium ALM parts, Conf. Ind. Comput. Tomogr. (2012), pp. 85–93 (Accessed 22 August 2017), http://www.ndt.net/article/ctc2012/papers/91.pdf.
[11] H.N. Chia, B.M. Wu, V. Cristini, J. Kim, J. Lowengrub, S. Singh, Recent advances in 3D printing of biomaterials, J. Biol. Eng. 9 (2015) 4, https://doi.org/10.1186/s13036-015-0001-4.
[12] T.B. Kim, S. Yue, Z. Zhang, E. Jones, J.R. Jones, P.D. Lee, Additive manufactured porous titanium structures: through-process quantification of pore and strut networks, J. Mater. Process. Technol. 214 (2014) 2706–2715, https://doi.org/10.1016/j.jmatprotec.2014.05.006.
[13] T.B. Sercombe, X. Xu, V.J. Challis, R. Green, S. Yue, Z. Zhang, P.D. Lee, Failure modes in high strength and stiffness to weight scaffolds produced by Selective Laser Melting, Mater. Des. 67 (2015) 501–508, https://doi.org/10.1016/j.matdes.2014.10.063.

[14] Y. Kok, X.P. Tan, P. Wang, M.L.S. Nai, N.H. Loh, E. Liu, S.B. Tor, Anisotropy and heterogeneity of microstructure and mechanical properties in metal additive manufacturing: a critical review, Mater. Des. 139 (2018) 565–586, https://doi.org/10.1016/J.MATDES.2017.11.021.
[15] W.J. Sames, F.A. List, S. Pannala, R.R. Dehoff, S.S. Babu, The metallurgy and processing science of metal additive manufacturing, Int. Mater. Rev. 6608 (2016) 1–46, https://doi.org/10.1080/09506608.2015.1116649.
[16] W.E. Frazier, Metal additive manufacturing: a review, J. Mater. Eng. Perform. 23 (2014) 1917–1928, https://doi.org/10.1007/s11665-014-0958-z.
[17] J.J. Lewandowski, M. Seifi, Metal additive manufacturing: a review of mechanical properties, Annu. Rev. Mater. Res. 46 (2016) 151–186, https://doi.org/10.1146/annurev-matsci-070115-032024.
[18] J.H. Martin, B.D. Yahata, J.M. Hundley, J.A. Mayer, T.A. Schaedler, T.M. Pollock, 3D printing of high-strength aluminium alloys, Nature 549 (2017) 365–369, https://doi.org/10.1038/nature23894.
[19] Y.M. Wang, T. Voisin, J.T. McKeown, J. Ye, N.P. Calta, Z. Li, Z. Zeng, Y. Zhang, W. Chen, T.T. Roehling, R.T. Ott, M.K. Santala, P.J. Depond, M.J. Matthews, A.V. Hamza, T. Zhu, Additively manufactured hierarchical stainless steels with high strength and ductility, Nat. Mater. 17 (2017) 63–71, https://doi.org/10.1038/nmat5021.
[20] Z. Sun, X. Tan, S.B. Tor, C.K. Chua, Simultaneously enhanced strength and ductility for 3D-printed stainless steel 316L by selective laser melting, NPG Asia Mater. 10 (2018) 127–136, https://doi.org/10.1038/s41427-018-0018-5.
[21] L. Thijs, F. Verhaeghe, T. Craeghs, J. Van Humbeeck, J.-P. Kruth, A study of the micro structural evolution during selective laser melting of Ti-6Al-4V, Acta Mater. 58 (2010) 3303–3312, https://doi.org/10.1016/j.actamat.2010.02.004.
[22] L.E. Murr, E. Martinez, K.N. Amato, S.M. Gaytan, J. Hernandez, D.A. Ramirez, P.W. Shindo, F. Medina, R.B. Wicker, Fabrication of metal and alloy components by additive manufacturing: examples of 3D materials science, J. Mater. Res. Technol. 1 (2012) 42–54, https://doi.org/10.1016/S2238-7854(12)70009-1.
[23] A.A. Antonysamy, J. Meyer, P.B. Prangnell, Effect of build geometry on the β-grain structure and texture in additive manufacture of Ti6Al4V by selective electron beam melting, Mater. Charact. 84 (2013) 153–168, https://doi.org/10.1016/j.matchar.2013.07.012.
[24] William Steen, Jyotirmoy Mazumder, Laser Material Processing, 4th ed., Springer-Verlag London, 1998, https://doi.org/10.1007/978-1-84996-062-5.
[25] M. Mahesh, B. Lane, A. Donmez, S. Feng, S. Moylan, R. Fesperman, Measurement Science Needs for Real-Time Control of Additive Manufacturing Powder Bed Fusion Processes, (2015), https://doi.org/10.6028/NIST.IR.8036.
[26] J.-P. Kruth, G. Levy, F. Klocke, T.H.C. Childs, Consolidation phenomena in laser and powder-bed based layered manufacturing, CIRP Ann. - Manuf. Technol. 56 (2007) 730–759, https://doi.org/10.1016/j.cirp.2007.10.004.
[27] S.K. Everton, M. Hirsch, P. Stravroulakis, R.K. Leach, A.T. Clare, Review of in-situ process monitoring and in-situ metrology for metal additive manufacturing, Mater. Des. 95 (2016) 431–445, https://doi.org/10.1016/j.matdes.2016.01.099.
[28] Y.-A. Song, W. Koenig, Experimental study of the basic process mechanism for direct selective laser sintering of low-melting metallic powder, CIRP Ann. - Manuf. Technol. 46 (1997) 127–130, https://doi.org/10.1016/S0007-8506(07)60790-2.
[29] M. Rombouts, J.-P. Kruth, L. Froyen, P. Mercelis, P. Merce, Fundamentals of selective laser melting of alloyed steel powders, CIRP Ann. - Manuf. Technol. 55 (2006) 187–192, https://doi.org/10.1016/S0007-8506(07)60395-3.
[30] J.-P. Kruth, P. Mercelis, J. Van Vaerenbergh, T. Craeghs, Feedback control of Selective Laser Melting, 3rd Int. Conf. Adv. Res. Virtual Rapid Prototyp. (2007) p. 7.
[31] T. Furumoto, M.R. Alkahari, T. Ueda, M.S.A. Aziz, A. Hosokawa, Monitoring of laser consolidation process of metal powder with high speed video camera, laser assist, Net Shape Eng. 39 (2012) 760–766, https://doi.org/10.1016/j.phpro.2012.10.098.
[32] P. Bidare, R.R.J. Maier, R.J. Beck, J.D. Shephard, A.J. Moore, An open-architecture metal powder bed fusion system for in-situ process measurements, Addit. Manuf. 16 (2017) 177–185, https://doi.org/10.1016/j.addma.2017.06.007.
[33] F. Bayle, M. Doubenskaia, Selective Laser Melting process monitoring with high speed infra-red camera and pyrometer, Proc. SPIE, International Society for Optics and Photonics (2008), https://doi.org/10.1117/12.786940 p. 698505.
[34] L. Thijs, K. Kempen, J.-P. Kruth, J. Van Humbeeck, Fine-structured aluminium products with controllable texture by selective laser melting of pre-alloyed AlSi10Mg powder, Acta Mater. 61 (2013) 1809–1819, https://doi.org/10.1016/j.actamat.2012.11.052.
[35] M.R. Alkahari, T. Furumoto, T. Ueda, A. Hosokawa, Consolidation characteristics of ferrous-based metal powder in additive manufacturing, J. Adv. Mech. Des. Syst. Manuf. 8 (2014) JAMDSM0009, , https://doi.org/10.1299/jamdsm.2014jamdsm0009.
[36] T. Furumoto, T. Ueda, M.R. Alkahari, A. Hosokawa, Investigation of laser consolidation process for metal powder by two-color pyrometer and high-speed video camera, CIRP Ann. - Manuf. Technol. 62 (2013) 223–226, https://doi.org/10.1016/j.cirp.2013.03.032.
[37] J.T. McKeown, K. Zweiacker, C. Liu, D.R. Coughlin, A.J. Clarke, J.K. Baldwin, J.W. Gibbs, J.D. Roehling, S.D. Imhoff, P.J. Gibbs, D. Tourret, J.M.K. Wiezorek, G.H. Campbell, Time-resolved in situ measurements during rapid alloy solidification: experimental insight for additive manufacturing, JOM (2016) 1–15, https://doi.org/10.1007/s11837-015-1793-x.
[38] E. Maire, P.J. Withers, Quantitative X-ray tomography, Int. Mater. Rev. 59 (2014) 1–43, https://doi.org/10.1179/1743280413Y.0000000023.
[39] M.P. Olbinado, X. Just, J.-L. Gelet, P. Lhuissier, M. Scheel, P. Vagovic, T. Sato, R. Graceffa, J. Schulz, A. Mancuso, J. Morse, A. Rack, MHz frame rate hard X-ray phase-contrast imaging using synchrotron radiation, Opt. Express 25 (2017) 13857, https://doi.org/10.1364/OE.25.013857.
[40] S. Zabler, A. Rack, F. García-Moreno, A. Ershov, T. Baumbach, J. Banhart, Imaging fast processes in liquid metal foams and semi-solid alloys using synchrotron radioscopy with spatio-temporal micro-resolution, In-Situ Stud. with Photons, Neutrons Electrons Scatt. Springer, 2010, pp. 149–158, https://doi.org/10.1007/978-3-642-14794-4_10.
[41] P.D. Lee, J.D. Hunt, Hydrogen porosity in directional solidified aluminium-copper alloys: in situ observation, Acta Mater. 45 (1997) 4155–4169, https://doi.org/10.1016/S1359-6454(97)00081-5.
[42] A.B. Phillion, R.W. Hamilton, D. Fuloria, A.C.L. Leung, P. Rockett, T. Connolley, In situ X-ray observation of semi-solid deformation and failure in Al – Cu alloys, Acta Mater. 59 (2011) 1436–1444, https://doi.org/10.1016/j.actamat.2010.11.005.
[43] T. Yamada, T. Shobu, A. Nishimura, Y. Yonemoto, S. Yamashita, T. Muramatsu, In-situ X-ray observation of molten pool depth during laser micro welding, J. Laser Micro Nanoeng. 7 (2012) 244–248, https://doi.org/10.2961/jlmn.2012.03.0002.
[44] C. Zhao, K. Fezzaa, R.W. Cunningham, H. Wen, F. Carlo, L. Chen, A.D. Rollett, T. Sun, Real-time monitoring of laser powder bed fusion process using high-speed X-ray imaging and diffraction, Sci. Rep. 7 (2017) 3602.
[45] C.L.A. Leung, S. Marussi, R.C. Atwood, M. Towrie, P.J. Withers, P.D. Lee, In situ X-ray imaging of defect and molten pool dynamics in laser additive manufacturing, Nat. Commun. 9 (2018) 1355, https://doi.org/10.1038/s41467-018-03734-7.
[46] Q. Guo, C. Zhao, L.I. Escano, Z. Young, L. Xiong, K. Fezzaa, W. Everhart, B. Brown, T. Sun, L. Chen, Transient dynamics of powder spattering in laser powder bed fusion additive manufacturing process revealed by in-situ high-speed high-energy x-ray imaging, Acta Mater. 151 (2018) 169–180, https://doi.org/10.1016/j.actamat.2018.03.036.
[47] N.P. Calta, J. Wang, A.M. Kiss, A.A. Martin, P.J. Depond, G.M. Guss, V. Thampy, A.Y. Fong, J.N. Weker, K.H. Stone, C.J. Tassone, M.J. Kramer, M.F. Toney, A. Van Buuren, M.J. Matthews, An instrument for in situ time-resolved X-ray imaging and diffraction of laser powder bed fusion additive manufacturing processes, Rev. Sci. Instrum. 89 (2018) 055101, https://doi.org/10.1063/1.5017236.
[48] J. Romano, L. Ladani, M. Sadowski, Thermal modeling of laser based additive manufacturing processes within common materials, Procedia Manuf. (2015) 238–250, https://doi.org/10.1016/j.promfg.2015.09.012.
[49] C.D. Boley, S.C. Mitchell, A.M. Rubenchik, S.S.Q. Wu, Metal powder absorptivity: modeling and experiment, Appl. Opt. 55 (2016) 6496, https://doi.org/10.1364/AO.55.006496.
[50] J.J. Valencia, P.N. Quested, Thermophysical properties, ASM Handb. Cast. vol. 15, (2008), pp. 468–481, https://doi.org/10.1361/asmhba0005240.
[51] Q. Fu, E. Saiz, A.P. Tomsia, Direct ink writing of highly porous and strong glass scaffolds for load-bearing bone defects repair and regeneration, Acta Biomater. 7 (2011) 3547–3554, https://doi.org/10.1016/j.actbio.2011.06.030.
[52] H. Ylänen, Bioactive Glasses: Materials, Properties and Applications, Woodhead Publishing Ltd, 2011, https://doi.org/10.1533/9780857093318.
[53] K.M. Kareh, P.D. Lee, R.C. Atwood, T. Connolley, C.M. Gourlay, Revealing the micromechanisms behind semi-solid metal deformation with time-resolved X-ray tomography, Nat. Commun. 5 (2014), https://doi.org/10.1038/ncomms5464.
[54] S. Karagadde, P.D. Lee, B. Cai, J.L. Fife, M.A. Azeem, K.M. Kareh, C. Puncreobutr, D. Tsivoulas, T. Connolley, R.C. Atwood, Transgranular liquation cracking of grains in the semi-solid state, Nat. Commun. 6 (2015) 8300, https://doi.org/10.1038/ncomms9300.
[55] Y.C. Fredholm, N. Karpukhina, R.V. Law, R.G. Hill, Strontium containing bioactive glasses: glass structure and physical properties, J. Non Cryst. Solids 356 (2010) 2546–2551, https://doi.org/10.1016/j.jnoncrysol.2010.06.078.
[56] Z.Y. Wu, R.G. Hill, S. Yue, D. Nightingale, P.D. Lee, J.R. Jones, Melt-derived bioactive glass scaffolds produced by a gel-cast foaming technique, Acta Biomater. 7 (2011) 1807–1816, https://doi.org/10.1016/j.actbio.2010.11.041.
[57] E. Ghadiri, S.M. Zakeeruddin, A. Hagfeldt, M. Grätzel, J.E. Moser, Ultrafast charge separation dynamics in opaque, operational dye-sensitized solar cells revealed by femtosecond diffuse reflectance spectroscopy, Sci. Rep. 6 (2016) 24465, https://doi.org/10.1038/srep24465.
[58] K. Dabov, A. Foi, V. Katkovnik, Image denoising by sparse 3D transformation-domain collaborative filtering, IEEE Trans. Image Process. 16 (2007) 1–16, https://doi.org/10.1109/TIP.2007.901238.
[59] C. Schneider, W.S. Rasband, K.W. Eliceiri, NIH Image to ImageJ: 25 years of image analysis, Nat. Methods 9 (2012) 671–675, https://doi.org/10.1038/nmeth.2089.
[60] S. Yue, P.D. Lee, G. Poologasundarampillai, J.R. Jones, Evaluation of 3-D bioactive glass scaffolds dissolution in a perfusion flow system with X-ray microtomography, Acta Biomater. 7 (2011) 2637–2643, https://doi.org/10.1016/j.actbio.2011.02.009.
[61] M.J. Matthews, G. Guss, S.A. Khairallah, A.M. Rubenchik, P.J. Depond, W.E. King, Denudation of metal powder layers in laser powder bed fusion processes, Acta Mater. 114 (2016) 33–42, https://doi.org/10.1016/j.actamat.2016.05.017.
[62] P.D. Lee, T. North, A.R. Perrin, Methods of experimental confirmation of a computational model of the fluid flow in gas tungsten arc welding, in: A.F. Giamei, G.J. Abbaschian (Eds.), Model. Control Cast. Weld. Process. IV, TMS, Florida, 1988, pp. 131–140.
[63] P. Kongsuwan, G. Brandal, Y. Lawrence Yao, Laser induced porosity and crystallinity modification of a bioactive glass coating on titanium substrates, J. Manuf. Sci. Eng. 137 (2015) 031004, https://doi.org/10.1115/1.4029566.
[64] H.S. Khatak, B. Raj, Corrosion of Austenitic Stainless Steels - Mechanism, Mitigation and Monitoring, Elsevier Science, 2002, https://doi.org/10.1533/9780857094018.
[65] L. Boccaccini, R. Aldo, Delia S. Brauer, Hupa, Bioactive Glasses - Foundamentals, Technology and Applications, Royal Society of Chemistry, 2016.
[66] S. Ly, A.M. Rubenchik, S.A. Khairallah, G. Guss, M.J. Matthews, Metal vapor microjet controls material redistribution in laser powder bed fusion additive manufacturing, Sci. Rep. 7 (2017) 4085, https://doi.org/10.1038/s41598-017-04237-z.
[67] P.D. Lee, A. Chirazi, D. See, Modeling microporosity in aluminum-silicon alloys: a

review, J. Light Met. 1 (2001) 15–30, https://doi.org/10.1016/S1471-5317(00)00003-1.
[68] A.M. Prokhorov, V.I. Konov, I. Ursu, I.N. Mihailescu, Laser Heating of Metals, IOP Publishing Ltd, Bristol, UK, 1990.
[69] J.T. Mcaloren, A reproducible magnesium oxide standard for reflectance measurement from 0.3 to 2.6μ, Nature 195 (1962) 797–798, https://doi.org/10.1038/195797a0.
[70] L. Naf, K. Doped, C. Rao, T. Srikumar, M. Rao, Physical and optical absorption studies on Li2O-Al2O3-P2O5 glasses doped with Sm2O3, Int. J. Sci. Res. 7 (2015) 420–425 (Accessed 3 August 2017), https://www.ijsr.net/conf/ATOM2014/ATOM2014_15.pdf.
[71] G. Ou, Z. Li, D. Li, L. Cheng, Z. Liu, H. Wu, Photothermal therapy by using titanium oxide nanoparticles, Nano Res. 9 (2016) 1236–1243, https://doi.org/10.1007/s12274-016-1019-8.
[72] M.M. Morsi, S.I. El-sherbiny, K.M. Mohamed, Spectroscopic investigation of amber color silicate glasses and factors affecting the amber related absorption bands, Spectrochim. Acta Part A Mol. Biomol. Spectrosc. 145 (2015) 376–383, https://doi.org/10.1016/J.SAA.2015.03.001.
[73] I. Zhirnov, R.S. Khmyrov, C.E. Protasov, A.V. Gusarov, Time-resolved visualization of laser beam melting of silica glass powder, Phys. Procedia 83 (2016) 1013–1020, https://doi.org/10.1016/j.phpro.2016.08.106.
[74] Q. Fu, M.N. Rahaman, B.S. Bal, W. Huang, D.E. Day, Preparation and bioactive characteristics of a porous 13-93 glass, and fabrication into the articulating surface of a proximal tibia, J. Biomed. Mater. Res. Part A 82A (2007) 222–229, https://doi.org/10.1002/jbm.a.31156.
[75] M.N. Ahsan, R. Bradley, A.J. Pinkerton, Microcomputed tomography analysis of intralayer porosity generation in laser direct metal deposition and its causes, J. Laser Appl. 23 (2011) 022009, https://doi.org/10.2351/1.3582311.
[76] E.C.K. Junjie Luo, Theresa Bender, Douglas Bristow, Robert Landers, Jonathan Goldstein, Augustine Urbas, Bubble formation in additive manufacturing of borosilicate glass, Solid Free Form Fabr. Symp. (2016) (Accessed 12 October 2017), http://www.programmaster.org/PM/PM.nsf/ApprovedAbstracts/9C4271459007A67985257FA20007A651?OpenDocument.
[77] C. Qiu, C. Panwisawas, M. Ward, H.C. Basoalto, J.W. Brooks, M.M. Attallah, On the role of melt flow into the surface structure and porosity development during selective laser melting, Acta Mater. 96 (2015) 72–79, https://doi.org/10.1016/j.actamat.2015.06.004.
[78] P.D. Lee, J.D. Hunt, Measuring the nucleation of hydrogen porosity during the solidification of aluminium-copper alloys, Scr. Mater. 36 (1997) 399–404, https://doi.org/10.1016/S1359-6462(96)00411-3.
[79] S.A. Khairallah, A.T. Anderson, A. Rubenchik, W.E. King, Laser powder-bed fusion additive manufacturing: physics of complex melt flow and formation mechanisms of pores, spatter, and denudation zones, Acta Mater. 108 (2016) 36–45, https://doi.org/10.1016/j.actamat.2016.02.014.
[80] J. Luo, H. Pan, E.C. Kinzel, Additive manufacturing of glass, J. Manuf. Sci. Eng. 136 (2014) 061024, https://doi.org/10.1115/1.4028531.
[81] M. Fateri, A. Gebhardt, Selective laser melting of soda-lime glass powder, Int. J. Appl. Ceram. Technol. 12 (2015) 53–61, https://doi.org/10.1111/ijac.12338.
[82] R.S. Khmyrov, C.E. Protasov, S.N. Grigoriev, A.V. Gusarov, Crack-free selective laser melting of silica glass: single beads and monolayers on the substrate of the same material, Int. J. Adv. Manuf. Technol. 85 (2016) 1461–1469, https://doi.org/10.1007/s00170-015-8051-9.
[83] C.E. Protasov, R.S. Khmyrov, S.N. Grigoriev, A.V. Gusarov, Selective laser melting of fused silica: interdependent heat transfer and powder consolidation, Int. J. Heat Mass Transf. 104 (2017) 665–674, https://doi.org/10.1016/j.ijheatmasstransfer.2016.08.107.
[84] K.C.R. Kolan, M.C. Leu, G.E. Hilmas, M. Velez, Effect of material, process parameters, and simulated body fluids on mechanical properties of 13-93 bioactive glass porous constructs made by selective laser sintering, J. Mech. Behav. Biomed. Mater. 13 (2012) 14–24, https://doi.org/10.1016/j.jmbbm.2012.04.001.
[85] K.C.R. Kolan, Selective Laser Sintering of Bioactive Glass Scaffolds and Their Biological Assessment for Bone Repair, Thesis Missouri University of Science and Technology, 2015 (Accessed 20 July 2017), https://search.proquest.com/docview/1762524981?pq-origsite=gscholar.